Interpretation of SOFIE PMC measurements: Cloud identification and derivation of mass density, particle shape, and particle size

Mark E. Hervig[a,]*, Larry L. Gordley[a], Michael H. Stevens[b], James M. Russell III[c], Scott M. Bailey[d] and Gerd Baumgarten[e]

[a]GATS, Inc., Driggs, Idaho, 83422, USA.

[b]Space Science Division, Naval Research Laboratory, Washington, DC 20375, USA.

[c]Hampton University, Hampton, VA, 23668, USA.

[d]Virginia Technical Institute, Blacksburg, VA, 24061, USA.

[e]Leibniz-Institute of Atmospheric Physics, University Rostock, Kühlungsborn, Germany7

*Corresponding author. E-mail address: m.e.hervig@gats-inc.com (M. Hervig).

Abstract. The Solar Occultation For Ice Experiment (SOFIE) was launched onboard the Aeronomy of Ice in the Mesosphere (AIM) spacecraft to measure polar mesospheric clouds (PMCs) and the environment in which they form. This work describes methods for identifying PMCs in SOFIE observations and determining mass density, particle shape, particle effective radius, and particle size distribution. Results using SOFIE measurements from the northern summer of 2007 are presented and compared to the observations by the ALOMAR RMR-lidar in northern Norway (69°N). SOFIE indicates that on average the mesospheric ice layer extends continuously from 81.0 to 87.4 km altitude, with the peak in extinction at 83.8 km. The peak altitude is consistent with the concurrent lidar measurements, but previous instruments indicate a narrower ice layer due to reduced sensitivity compared to SOFIE. SOFIE indicates an average ice mass density of ~15 ng m^{-3} at the peak altitude, about a factor of three less than concurrent lidar observations and previous observations. This difference is due in part to the increased sensitivity of SOFIE compared to other instruments, and in part to averaging by the relatively large SOFIE sample volume. The SOFIE infrared (IR) extinction spectra are used to infer PMC particle shape, where aspherical particles are assumed to be oblate or prolate spheroids. The particle axial ratio inferred at the extinction peak ranges from about 1.3 to 3 with an average of 2.2. The effective radius of PMC particles determined at the extinction peak altitude is ~36 nm, in good agreement with concurrent lidar measurements which indicate ~38 nm. SOFIE results at the extinction peak give Gaussian size distributions with an average concentration of 374 cm^{-3}, median radius of 29.0 nm, and width of 11.8 nm. Concurrent ALOMAR lidar results are in generally good agreement with an average concentration of 228 cm^{-3}, median radius of 40.4 nm, and width of 12.1 nm. The SOFIE average suggests higher concentrations of smaller particles due to the detection of median radii smaller than ~18 nm, which are not observed by the lidar. Ice particle properties determined from SOFIE are in good agreement with the concurrent ALOMAR lidar observations, taking the different instrument characteristics into account. Inter-comparisons with concurrent lidar and previous satellite and ground-based measurements validate the SOFIE retrieval methods and demonstrate the high fidelity of SOFIE measurements.

Keywords: AIM; SOFIE; mesosphere; PMC

1. Introduction

AIM is the first satellite mission dedicated to measuring PMCs and the environment in which they form (Russell et al., 2008). It was launched into a 600 km circular polar orbit on 25 April 2007, and is intended to operate for at least two years. The AIM observatory is comprised of the Solar Occultation For Ice Experiment (SOFIE), the Cloud Imaging and Particle Size (CIPS) experiment, and the Cosmic Dust Experiment (CDE). The focused AIM observations are providing increased understanding of PMCs that in turn will improve our understanding of long-term (>10 year) variations. This work describes the use of SOFIE measurements to identify PMCs and determine ice mass density, particle shape, particle effective radius, and particle size distribution. These physical quantities are versatile in scientific studies and offer a basis for comparison with models and different measurement techniques and wavelengths. Results from SOFIE PMC measurements in the northern polar summer of 2007 are presented and compared to previous and concurrent results.

2. SOFIE Observations

SOFIE uses the technique of satellite solar occultation to measure vertical profiles of limb path atmospheric transmission within 16 spectral bands between 0.29 and 5.32 μm wavelength (Gordley et al., 2008, this issue). Occultation measurements are accomplished by monitoring solar intensity as the satellite enters or exits the Earth's sunlit side. The ratio of solar intensity measured through the atmosphere (V) to the intensity measured outside the atmosphere (V_0) yields atmospheric transmission, $\tau = V/V_0$, which is the basis for retrieving the desired geophysical parameters. SOFIE measurements are used to retrieve PMC extinction, $\beta(\lambda)$, at eleven wavelengths (λ) from 0.330 to 5.01 μm, in addition to temperature and the abundance of five gaseous species (O_3, H_2O, CO_2, CH_4, and NO). PMCs are measured by monitoring the attenuation of solar energy using broadband radiometers. In addition, SOFIE measures the radiometer difference signal for band pairs that are close in wavelength. Difference signals allow the advantage of electronic gain which permits digitization of small signals that are near the detector noise. The digitization limit for the radiometer PMC measurements corresponds to 10^{-7} km^{-1} in extinction. Laboratory and on-orbit characterization of the radiometer PMC measurement channels indicate measurement noise of about 2×10^{-8} km^{-1}. PMC difference signals measured in channel 2 (0.867 and 1.037 μm wavelengths) have a digitization limit corresponding to ~4×10^{-10} km^{-1} and a measured noise level of ~6×10^{-10} km^{-1}. This work uses PMC extinctions retrieved from the channel 2 difference signals, which yield the extinction at

1.037 µm. In this work we take the radiometer PMC noise level (β_{noi}) as the digitization limit (β_{noi} = 10^{-7} km^{-1}). The SOFIE field of view is about 1.5 km vertical × 4.3 km horizontal. Detectors are sampled at 20 Hz which corresponds to ~145 m vertical spacing, or roughly 10 times over-sampling. The sample volume length, as defined by the line-of-sight entrance and exit of a spherical shell with vertical thickness of the FOV, is ~290 km. SOFIE observes 15 sunsets in the southern hemisphere and 15 sunrises in the northern hemisphere each day. Measurement latitude coverage ranges from about 65° to 80° north or south. Because AIM is in a retrograde orbit, SOFIE sunset (sunrise) observations occur near the time of local sunrise (sunset). See Gordley et al. (2008, this issue) for a complete description of the SOFIE experiment.

3. Background: Physical and Optical PMC Properties

Simulations of PMC extinction require the particle refractive index, calculated particle optical cross sections, and the particle size distribution. This section reviews the relevant topics and covers important details related to interpreting SOFIE measurements.

3.1. Particle Size

Interpreting SOFIE measurements requires knowledge of the appropriate particle size regime to consider. PMC size distributions have been treated using the lognormal form in the majority of PMC research. The lognormal distribution is described by the total concentration (N) median radius (r_m) and width, (σ, dimensionless). On the other hand, Rapp and Thomas (2006) recently demonstrated that microphysical model calculations of PMC size distributions are most accurately described using a Gaussian size distribution, which is described by the total concentration, median radius, and distribution width (Δr, units of length). We also consider the effective radius, $r_e = \int r^3 n(r)\mathrm{d}r \,/\, \int r^2 n(r)\mathrm{d}r$, where $n(r)$ is the radius-dependent concentration.

While r_e can be determined for any size distribution (i.e., lognormal or Gaussian), it is not inherently related to a specific functional form. Thus, r_e offers a representation of particle size that is independent of the assumed form of the size distribution. The current record of lognormal size distributions (e.g., Rusch et al., 1991; von Cossart et al., 1999; Alpers et al., 2000; Debrestian et al., 1997) suggest $20 < r_m = < 74$ nm, $1.2 < \sigma < 1.7$, and $23 < N < 1078$ cm^{-3}, with r_e from 38 to 86 nm. The average of 11 distributions from von Cossart et al. (1999) was reported as $r_m = 51$ nm, $\sigma = 1.42$, and $N = 82$ cm^{-3}, with $r_e = 69$ nm. Rapp and Thomas (2006) reported Gaussian fits to 33 modeled PMC size distributions which spanned $9 < N < 421$ cm^{-3}, $24 < r_m < 84$ nm, and $9 < \Delta r < 27$ nm ($32 < r_e < 101$ nm). The median distribution values from Rapp and Thomas are $N = 139$ cm^{-3}, $r_m = 41$ nm, and $\Delta r = 13$ nm, with $r_e = 48$ nm. A recent report using 10 years of lidar PMC measurements over ALOMAR in northern Norway (69°N, 16°E) indicates gaussian size distributions with $33 < N < 105$ cm^{-3}, $42 < r_m < 62$ nm, and $15 < \Delta r < 18$ nm ($52 < r_e < 71$ nm) (Baumgarten et al., 2008). Rusch et al. (2007) used Solar Mesosphere Explorer (SME) and the Student Nitric Oxide Explorer (SNOE) data to determine gaussian distributions assuming $\Delta r = 14$ nm. Results based on SME indicate r_m from 20 to 70 nm (r_e from 34 to 75 nm) and SNOE results indicate r_m from 10 to 50 nm (r_e from 27 to 52 nm). In summary, the above measurements and models suggest r_e from 27 to 101 nm, regardless of the assumed size distribution.

3.2. Particle Shape

Historically, both microphysical and optical modeling of PMCs have assumed that the particles can be treated as spheres. However, recent efforts have suggested that PMC particles are indeed non-spherical. In general, these efforts have treated non-spherical particles as randomly oriented spheroids. Particle axial ratio (AR) denotes the length-to-diameter ratio of a spheroid, with $AR > 1$ corresponding to oblate spheroids (AR_O) and $AR < 1$ to prolate spheroids (AR_P). Baumgarten et al. (2002) showed that polarization sensitive ground-based lidar measurements of PMCs indicate 1.7% depolarization, and suggested that this signal was consistent with particles having AR in excess of 2.5. Eremenko et al. (2005) demonstrated that high resolution infrared (IR) PMC spectra from the satellite-borne Atmospheric Chemistry Experiment (ACE) were more readily explained by modeled extinctions considering randomly oriented prolate or oblate spheroids, than by extinctions calculated for spherical particles. Their work suggests that PMC particles are consistent with AR of about 2.0. Using both ground-based and satellite observations, Rapp et al. (2007) concluded that measured optical PMC properties were best explained using randomly oriented spheroids with AR of either about 0.2 or 5.0. In summary, previous results indicate that observations are consistent with AR_O between about 2 and 5 (AR_P between 0.2 and 0.5).

2.3. Ice Refractive Index

Under typical PMC conditions (temperature < ~150 K, roughly 0.006 hPa pressure) cubic ice (Ic) is probably the preferred habit (Petrenko and Whitworth, 1999). The current record of available ice refractive indices is predominantly for hexagonal ice (Ih), with only a few measurements at limited wavelengths for cubic ice. Warren (1984) suggested that the optical properties of hexagonal and cubic ice can be considered identical, however, the existing data are insufficient to validate that assertion. The refractive indices of hexagonal ice used in this work are summarized in Table 1 and compared in Fig. 1 for SOFIE wavelengths greater than 2.4 µm. At wavelengths shorter than 2.4 µm the only available data re the room temperature results from Warren (1984). The data indicate temperature dependence that is generally consistent among the various data sets. Temperature dependence in the refractive index was captured using second order polynomial fits. The Gosse et al. (1995) indices were not included in these fits because they are sometimes vastly different from the other results, particularly within the 3 μm region (Fig. 1). The only opportunity to compare indices from all references is at 2.62 μm. Here the data suggest little or no temperature dependence in either the real or imaginary index. While the Clapp et al. (1995) indicate variation in temperature, the changes appear more random than physical in character than at the other SOFIE wavelengths. Including the Clapp et al. imaginary indices at 2.62 μm causes 100% uncertainty in the resulting polynomial fit. Because the other imaginary indices at 2.62 μm are generally consistent, the Clapp et al. results were not included in the polynomial fit at this wavelength. While a broad temperature dependence appears to be a consistent feature in the refractive index data, scatter among the various data would cast doubt on an attempt to capture this dependence within the range of expected PMC temperatures (roughly 130 - 150 K). Thus, the approach taken here was to use the refractive index at a fixed temperature (145 K) taken from polynomial fits to the various measurements. This approach (e.g., Fig. 1) was used for wavelengths greater than 2 μm and the resulting indices and their uncertainties are given in Table 2. Because temperature dependence at shorter wavelengths cannot be addressed from the available data, the indices from Warren (1984) at 266 K were used for wavelengths from 0.291 to 1.04 μm (Table 2).

3.4. Optical Calculations

Calculations of scattering and absorption by spheres are generally accomplished using Mie theory. This work treated non-spherical particles as randomly oriented spheroids and computed extinction cross sections using the T-matrix method of Mishchenko and Travis (1998). The size of a non-spherical particle is referenced using the radius of an equivalent-volume sphere. Ice particle scattering, absorption, and extinction cross sections are shown in Fig. 2a for

λ = 3.064 μm. At infrared wavelengths scattering is unimportant for particle radii less than about 200 nm. As a consistency check, extinction cross sections for spheres from the Mie and T-matrix algorithms are compared in Fig. 2b. The result for spherical particles from Mie theory is in perfect agreement with the T-matrix results for spheres. The cross sections for oblate and prolate spheroids have a constant offset compared to spherical particles with equivalent volume, for radii (r) less than about 200 nm. This difference results in constant offsets among PMC extinctions calculated for various particle shapes and the same size distribution. Simulated PMC absorption (β_A), scattering (β_S), and extinction ($\beta = \beta_A + \beta_S$) coefficients at the SOFIE wavelengths are shown in Fig. 3 for a relevant PMC particle size distribution. These results indicate that SOFIE PMC extinctions are dominated by scattering at wavelengths less than about 1.5 μm, while absorption dominates at wavelengths greater than about 2.5 μm.

4. Derivation of Physical PMC Properties

4.1. Ice Mass Density

Since absorption varies as r^3, IR PMC extinction is directly proportional to ice volume density (V_{ice}). Model calculations were used to quantify the relationship between extinction and V_{ice}. The calculations used ice refractive indices from Table 2 and considered a range of Gaussian size distributions with r_m from 10 to 100 nm, and Δr from 5 to 25 nm. For each size distribution used in the calculations, separate results were obtained for particle aspect ratios from 0.2 to 5. Fig. 4a shows the volume-extinction relationship considering spherical particles for band 10, and a fit to these data,

$$V_{ice} = A(\lambda)\,\beta(\lambda) \quad (1)$$

While sensitivity to particle size is generally small within the IR, the value of $A(\lambda)$ at certain wavelengths is sensitive to particle shape. Fig. 4b shows $A(\lambda)$ as a function of AR_O and AR_P.

Values of $A(\lambda)$ for prolate spheroids are shown versus $1/AR_P$, which demonstrates that the value of $A(\lambda)$ for an oblate spheroid closely approximates the value for a prolate spheroid with $AR_P \approx 1/AR_O$. The effect of varying axial ratio was captured using a linear fit to $A(\lambda)$ versus AR,

$$A(\lambda) = A_0(\lambda) + (AR\text{-}1)\, B(\lambda) \tag{2}$$

where $A_0(\lambda)$ corresponds to the value of $A(\lambda)$ for spheres and AR is either AR_O or $1/AR_P$. Values of $A_0(\lambda)$ and $B(\lambda)$ are given in Table 3. $A_0(\lambda)$ was determined as the average ratio of modeled volumes and extinctions considering r_m from 10 to 100 nm, and Δr from 5 to 25 nm. The uncertainty in $A(\lambda)$ due to the unknown particle size is independent of AR, and was taken as the standard deviation of the results. Assuming a lognormal rather than gaussian size distribution does not change the results. The uncertainty in $A(\lambda)$ due to the dependence on AR, or more specifically the slope $B(\lambda)$, was taken from the standard error in the regression to $A(\lambda)$ versus AR. Uncertainty in $A(\lambda)$ due to the refractive index was characterized by inducing random and independent variations in the real and imaginary indices (based on the uncertainties in Table 2) in a Monte Carlo simulation. The total uncertainty in $A(\lambda)$, δA, was found by combining (root-sum-squared) the uncertainties due to size, AR, and refractive index (see Table 3).

The total error in V_{ice} determined using SOFIE is a combination of the extinction measurement error, $\delta\beta$, and the uncertainty in $A(\lambda)$. For random measurement errors the uncertainty in V_{ice} can be written as $\delta V_{ice} = [\delta\beta^2 + \delta A^2]^{1/2}$. The constants for bands 5-7 have large uncertainties and thus are not recommended for inferring V_{ice}. For SOFIE PMC measurement wavelengths greater than 2.8 μm, δA is less than 5%. For PMC extinction measurement errors of 10%, the total uncertainty in V_{ice} is therefore less than 11%. The lowest theoretical uncertainties and shape sensitivity are found in bands 9 and 10. Since these channels also have the largest

PMC signals (Fig. 4), they are the most reliable measurements for determining PMC volume densities.

Ice mass density, M_{ice}, can be determined from V_{ice}

$$M_{ice} = C\, V_{ice}\, \rho_i \tag{3}$$

where ρ_i is the density of ice (0.93 g cm^{-3}, Pruppacher and Klett, 1997) and C is a units conversion constant. For V_{ice} in μm^3 cm^{-3} and ρ_i in g cm^{-3}, using C = 1000 gives M_{ice} in ng m^{-3}. The vertical column ice abundance (or ice water content, *IWC*) is determined from the vertical integral of M_{ice}.

4.2. Particle Shape

The dependence of PMC extinction on particle shape varies with wavelength. Because the extinction spectrum is also affected by particle size, particle shape characterization is best accomplished using a measure that is insensitive to size. The ratios of extinction at various SOFIE wavelengths were used to examine signals related to particle shape. Because wavelengths shorter than ~2 μm are very sensitive to particle size, measurements within the IR were chosen. Within the infrared PMC extinctions are generally insensitive to particle size and thus offer the ability to determine particle shape without knowledge of size. Example calculations are shown in Fig. 5a, where the band 9 / 10 extinction ratio, $R_{910} = \beta(3.064)/\beta(3.186)$, is shown versus median radius for various axial ratios. The extinction ratio is only slightly sensitive to particle size, but varies notably for the *AR* considered. Fig. 5b shows the calculated extinction ratio versus axial ratio as the average for r_m from 10 to 100 nm. The calculations did not address *AR* < 0.15 because the T-matrix solutions become unstable for large *AR* and small radii for IR wavelengths. The uncertainty in extinction ratio was determined as a combination of the variability over r_m from 10 to 100 nm and uncertainties due to refractive index. Total uncertainties in modeled $\beta(3.064)/\beta(3.186)$ are less than 3% as indicated in Fig. 5b. The extinction ratio – AR relationship in Fig. 5b is characterized by two solutions when AR is less than about four. If the T-matrix results could be obtained for $AR < 0.15$, it is likely that a corresponding prolate solution would exist for $AR > 4$. For a given extinction ratio, the prolate spheroid solutions can be approximated by the oblate spheroid axial ratios, i.e. $AR_P \approx 1/AR_O$. This relationship is typical of all SOFIE wavelength combinations. The total theoretical error in AR was determined from the range in AR inferred for a given extinction ratio considering extinction ratio errors as in Fig. 5b. The results (Fig. 5c) indicate less than 15% errors in AR for ~1.3 < AR < ~0.7 and greater than 60% errors when AR is close to unity.

SOFIE wavelength combinations suitable for identifying particle shape were chosen as those with large dynamic range in extinction ratio, low uncertainty due to refractive index, and low sensitivity to particle size. Dynamic range is defined using the range in extinction ratio for AR between 1 and 9. The sensitivity to refractive index or particle size is defined as the respective uncertainty in extinction ratio divided by the dynamic range as defined above. The extinction ratios $\beta(3.186)/\beta(2.939)$, $\beta(3.064)/\beta(3.384)$, and $\beta(3.064)/\beta(4.646)$ are suitable for determining axial ratio and have characteristics similar to those for $\beta(3.064)/\beta(3.186)$ presented here. In all cases, the extinction ratio versus AR curves yield two solutions for a given extinction ratio. The possibility that combining many wavelengths would define a unique aspect ratio was investigated, but the results indicate that roughly the same pairs of oblate and prolate aspect ratios are given by all four extinction ratios. Nevertheless, this approach will give height resolved information concerning particle shape. While PMCs could be composed of particles with varying AR, SOFIE measurements yield a mass weighted average over the sampled volume.

4.3. Effective Radius

PMC effective radius (r_e) can be determined independent of the size distribution using a combination of SOFIE near-IR and IR measurements. The relationship between the band 9 / band 3 extinction ratio, $R_{93} = \beta(3.064)/\beta(0.867)$, and r_e is shown in Fig. 6a based on model calculations considering particles with $AR = 2$ and Gaussian size distributions with $2 < r_m < 150$ nm and $5 < \Delta r < 20$ nm. These results were fit according to

$$\log(r_e) = a_1 + a_2 \log(R_{ab}) + a_3 \log^2(R_{ab}) + a_4 \log^3(R_{ab}) + a_5 \log^4(R_{ab}) \quad (4)$$

where r_e is in nm, R_{ab} is the ratio of extinction from band a and band b, and the constants a_1, a_2, a_3, a_4, and a_5 are given in Table 4 for various axial ratios of oblate spheroids. The extinction ratio $R_{94} = \beta(3.064)/\beta(1.037)$ gives results similar to those in Fig. 6, and the constants in (4) are given in Table 4 for both R_{93} and R_{94}. The constants in Table 4 are applicable to prolate spheroids with $AR_P = 1/AR_O$. The uncertainty in r_e due to the fit of r_e versus R_{94} is less than 8% for $3 < r_e < 150$ nm (Fig. 6b). The uncertainties in Fig. 6b are nearly identical to those determined for other axial ratios. The sensitivity of r_e to particle shape is shown in Fig. 6c, where r_e determined for $AR = 2$ is compared to that determined for $AR = 1$ or 3. The value of r_e varies by less than 2% for $r_e > 10$ nm and axial ratios between 1 and 5. While the effect of particle shape can be safely ignored, it could be captured by determining r_e versus AR and interpolating linearly to the known AR for a given measurement. Errors in effective radii determined from SOFIE measurements are a combination of the theoretical errors as shown in Fig. 6b with the appropriate measurement errors.

4.4. Size Distribution

SOFIE multi-wavelength PMC measurements can be used to retrieve Gaussian size distributions. SOFIE channel pairs are used to form extinction ratios, which are a function of the size distribution shape (median radius and width) alone. The size distribution retrievals were found to be relatively insensitive to particle shape, and the results presented here all assume $AR = 2$. For each measured extinction ratio all combinations of r_m and Δr are found that reproduce that measurement. An example is shown in Fig. 7a where extinction ratios were calculated for r_m = 38.5 nm and Δr = 16 nm and the curves represent all pairs of r_m and Δr that can explain an extinction ratio. While solutions are numerous for one channel pair, a unique solution can be found where the solutions from many channel pairs converge. In the example in Fig. 7a, the solution curves for extinction ratios using bands 2, 3, and 9 are found to converge at a unique combination of r_m and Δr. Contrast among the three solution curves indicates that the retrieved size distribution lies within a sharply defined minima (Fig. 7b). Once r_m and Δr are found, the total particle concentration is determined from the ratio of measured extinction (β_{meas}) at one wavelength to the simulated extinction (β_{sim}) using the retrieved r_m and Δr with $N = 1$ cm^{-3}.

$$N = \beta_{meas}(\lambda) \,/\, \beta_{sim}(\lambda, r_m, \Delta r, N = 1) \quad (5)$$

In practice N is determined using band 9, which has the highest signal-to-noise of all SOFIE PMC measurements. Error analysis of retrievals using synthetic band 2, 3, and 9 extinctions with 1% measurement errors indicate less than 3% errors in N, r_m, and Δr , for all possible combinations of r_m from 10 to 150 nm and Δr from 5 to 25 nm.

SOFIE band 2 signals appear to be saturating the pre-amplifier electronics (as discussed by Gordley et al., 2008, this issue), and are unusable except in a special operational mode. In the absence of band 2, well defined size distribution retrievals are not possible because insufficient contrast exists among the extinctions at wavelengths greater than 0.8 μm. While useful band 2 data are periodically collected, these measurements require more detailed analysis and we proceed without the band 2 PMC measurements. A common approach when the inversion is ill-defined is to derive the median radius and particle concentration for an assumed distribution width. However, SOFIE measurements provide information that can constrain the distribution width to a range of values that is perhaps more meaningful than an assumed number. Fig 8a shows the calculated extinction ratio $\beta(3.064)/\beta(1.037)$ versus median radius for discrete widths, which indicate that larger extinction ratios correspond to a narrower range of possible widths and median radii. To guide the discussion, the probability distribution of extinction ratio from SOFIE measurements at the altitude of peak extinction (Z_{max}) in the northern hemisphere during 2007 is overlain in Fig. 8a. SOFIE observations are characterized by $50 < \beta(3.064)/\beta(1.037) < 20000$, which corresponds to r_m from about 5 to 90 nm regardless of distribution width. The retrieval approach taken here determines the range of r_m versus Δr corresponding to a measurement of $\beta(3.064)/\beta(1.037)$, and the retrieved size distribution corresponds to the midpoint of the possible widths. The inversions allow Δr from 5 to 30 nm and $r_m > 5$ nm, consistent with previous observations (e.g. Baumgarten et al., 2008). Example results are shown in Fig 8b for calculated extinction ratios characteristic of the SOFIE observations. While the obvious limitation is choosing the midpoint from a broad range of solutions, results using SOFIE measurements are demonstrated below to be consistent with concurrent lidar results. Errors in retrieved N, r_m, and Δr were determined for inversions considering measurements simulated using r_m from 5 to 100 nm and Δr from 5 to 25 nm. The analysis considered only values of $\beta(3.064)/\beta(1.037)$ consistent with the SOFIE observations (50 to 20000). The results (Fig. 9) indicate uncertainties of less than 50% in N, r_m, and Δr for r_m from about 20 to 50 nm, depending on width. While the uncertainties can be large, the approach does provide meaningful constraints on the size distribution and offers lower uncertainties than when simply assuming a constant Δr. Future efforts will use the occasional UV PMC measurements from band 2 to perform well constrained inversions, and validate the approximations presented here.

5. PMC Identification

Ice layers are identified in SOFIE profiles when the measured band 9 / 10 extinction ratio is within the modeled range for PMCs (1.3 to 2.4, see Fig. 5b) and the bands 9 and 10 extinctions are both greater than the noise ($\beta_{noi} = 10^{-7}$ km^{-1}). Because $\beta(3.064)/\beta(3.186)$ is generally about 2, the threshold for ice detection becomes $\beta(3.064) > 2\times10^{-7}$ km^{-1}. An example is shown in Fig. 10, where the base of the ice layer (Z_{bot}) is identified at 79.5 km, the top of the ice layer (Z_{top}) at 90.8 km, and the altitude of peak extinction (Z_{max}) at 83.6 km. At Z_{max} in Fig. 10 the particle effective radius was 38 nm with an axial ratio of either 0.4 or 2.4.

Previous results indicate peak PMC altitudes from roughly 80 to 85 km at northern latitudes (e.g., Fiedler et al., 2004). SOFIE occasionally indicates PMCs with Z_{max} at lower altitudes, which is inconsistent because mesospheric temperatures are typically above the frost point below roughly 80 km. Anomalously low cloud detections can be explained by isolated clouds located within the line of sight (LOS) but far from the tangent point. This effect is illustrated in Fig. 11a, where the LOS at both 83 and 70 km tangent altitude is shown intercepting a cloud layer centered at 83 km altitude. When a cloud is spherically symmetric, uniform, and fills the FOV vertically, the tangent path length through the cloud (290 km) is defined by the LOS entrance and exit of the 1.5 km thick atmospheric shell. The illustration in Fig. 11a ignores ice layers above the tangent altitude because signal from these layers is removed in the recursive downward onion-peel retrievals. As evident in Fig. 11a, the path length through the cloud is reduced with decreasing tangent altitude. SOFIE PMC observations from the 2007 NH season were examined to understand anomalously low detection altitudes. PMC extinctions on a given day were normalized to the median extinction at Z_{max} for a given day, and the results are shown versus Z_{max} in Fig. 11b. SOFIE results are compared to the theoretical reduction in path length versus detection altitude, calculated assuming that clouds exists only on one side of the tangent point. The observed reduction in PMC extinction versus detection altitude is generally explained by theory, confirming that anomalously low detection altitudes are consistent with isolated clouds within the near or far extent of the LOS. The probability distribution of PMC Z_{max} for northern 2007 observations (Fig. 11c) indicates that most PMCs are observed between 80 and 90 km. In the current analysis of SOFIE observations, PMCs with Z_{max} below 79 km are considered anomalous and the measurement is discarded. This criteria eliminates about 14% of the SOFIE observations. In addition, SOFIE profiles can sometimes remain consistent with ice well below Z_{max}. These observations have not been seen by lidar, radar or rockets and are inconsistent with temperatures above the frost point at such low altitudes, but can be explained by isolated ice layers within the near or far extent of the LOS. Thus when interpreting SOFIE ice observations, values of Z_{bot} extending below ~79 km are likely erroneous. In future efforts, inhomogeneous cloud layers will be treated rigorously using coincident PMC imagery from CIPS to characterize the exact spatial cloud distributions.

PMC extinction is vertically smoothed by the SOFIE FOV which has a full-width half-maximum of about 1.5 km. SOFIE is designed so that all channels view the same volume of air simultaneously, minimizing the error in the ratios of retrieved extinction profiles. However, the FOV does limit the vertical resolution of retrieved extinction to about 1.5 km, which can impact the inference of particle characteristics if they vary substantially over 1.5 km or smaller height intervals. Consequently, our results are the optical extinction weighted mean over the 1.5 km FOV. This is further complicated by the non-uniform distribution of the cloud over the spherical layer. Simulations show that this effect is statistically minimal at and above the altitude of peak extinction. However, ultimate interpretation of results below the peak, due to the spherical geometry of the measurement, will require combined use of the CIPS images to allow selection of data with relative uniformity of cloud along the SOFIE line of sight.

The effects of vertical FOV smoothing were assessed by computing 3.064 μm extinction from CARMA model PMC size distribution profiles and smoothing the resulting profile over the SOFIE band 9 FOV function. An example result is shown in Fig. 12, where the extinction profile after smoothing over the SOFIE FOV depicts cloud top (base) roughly 1 km above (below) the original levels, where cloud top and base are taken as the levels where $\beta(3.06) = \beta_{noi}$. The displacement of cloud top and bottom altitudes is highly dependent on the vertical gradient in extinction, and the results in Fig. 12 will vary for different initial profiles. In this example, Z_{max} is displaced upward by about 0.5 km, and the magnitude of the extinction peak is reduced by about 30%. The absolute change in extinction is within ±30% at altitudes between roughly the original cloud base and top. These instrumental effects are unavoidable, but the induced errors are straight-forward to model and can be taken into account when interpreting SOFIE observations. Future efforts will address FOV de-convolution to partially remove the inherent vertical smoothing from the retrieved extinctions.

6. Results

SOFIE observations from the 2007 northern polar summer were analyzed to identify ice layers and determine microphysical properties. Measurement latitude varied from about 66° to 80°N during the PMC season with an average latitude of 68.9°N. SOFIE collected 1303 observations in the northern hemisphere from 20 May thru 2 September, and ice was detected in 82% of these. Observations with clouds having Z_{max} below 79 km were excluded from the results presented herein. SOFIE results are compared to PMC measurements from the ALOMAR lidar (69°N) during 2007, as described by Baumgarten et al. (2008). The three-color lidar measurements were used to determine cloud altitudes, Gaussian size distributions, and particle shape as the axial ratio of a cylinder. Physical cloud properties were determined from the lidar data at Z_{max} for comparison to SOFIE results. The lidar resolution is 50 m vertically by about 30 km horizontally. SOFIE and lidar results are summarized in Table 5 for the 2007 cloud season.

Probability distributions of SOFIE ice layer top, peak, and base altitude are shown in Fig. 13a. The histograms of Z_{bot} and layer thickness exclude observations of Z_{bot} < 79 km. SOFIE indicates ice layer tops occasionally above 90 km, with an average value of 87.6 km. This result is consistent with current understanding of temperatures and water vapor content at these altitudes (Lübken, 1999), and the associated ice particles at high altitudes are likely related to polar mesosphere summer echoes (e.g. Rapp et al., 2004). The lidar results indicate an average Z_{top} of 84.4 km, about 3 km lower than SOFIE. Vertical smoothing by SOFIE can cause an overestimate in Z_{top} of up to ~1 km, and therefore cannot explain this difference entirely. Baumgarten et al. (2008b) show that particle size decreases as concentration increases towards higher altitudes. Because the lidar signal varies as r^6 and SOFIE IR extinctions as r^3, the lidar signal would be expected to decrease more rapidly towards higher altitude than the IR SOFIE signal. Thus, SOFIE – lidar differences in Z_{top} are likely due to differing sensitivity of the two instruments. The average SOFIE Z_{max} (83.8 km) is 0.5 km higher than the lidar value (83.3 km), a difference that could be explained by vertical smoothing by SOFIE (see section 5), or may be due to the SOFIE data set containing ice layers with Z_{max} at higher altitudes than observed by the lidar. SOFIE indicates Z_{bot} from ~87 km to as low as 70 km, with an average value of 81.9 km. For typical temperature profiles, ice is not expected below ~79 km and observations of Z_{bot} < 79 km were excluded. Note that when isolated near or far field clouds exist within the SOFIE line of sight, they give the appearance of ice extending down to anomalous altitudes. The average lidar Z_{bot} was 82.2 km, slightly higher than SOFIE but within the mutual standard deviations (Table 5). The occasional occurrence of Z_{bot} at altitudes above ~85 km occurs when isolated ice layers are observed with Z_{max} located near the mesopause. SOFIE indicates ice layer thickness ($\Delta Z = Z_{top} - Z_{bot}$, Fig. 13b) ranging from 1 to 12 km with an average value of 5.6 km. Effects of the SOFIE FOV, as discussed above, can determine that SOFIE Z_{top} is overestimated by up to 1 km and that Z_{bot} is underestimated by up to 1 km. Accordingly, SOFIE ice layer thicknesses could be overestimated by up to 2 km. The lidar indicates an average ΔZ of 2.2 km, with differences from SOFIE primarily related to differences in Z_{top} as discussed above. SOFIE results were compared to model ice profiles from the Community Aerosol and Radiation Model for Atmospheres (CARMA; see Rapp and Thomas, 2006) initialized using temperature, water vapor and vertical wind profiles near 70° N from a global chemical-dynamical model (CHEM2D) representative of solar minimum and solar maximum conditions (Siskind et. al., 2005), and cloud lifetimes from 24 to 96 hours. The CARMA profiles were used to locate Z_{top} and Z_{bot} by finding the altitude where β_{noi} (10^{-7} km^{-1}) occurs. Identifying the SOFIE threshold in CARMA indicates $Z_{top} = 88.5 \pm 0.5$ km, $Z_{bot} = 82.5 \pm 0.6$ km, and a layer thickness from about 4 to 8 km. These results are consistent with the SOFIE observations considering the SOFIE error bars and systematic errors due to vertical smoothing by the SOFIE FOV.

Ice mass densities were derived from $\beta(3.06)$ and the measured axial ratios using equations 1 - 3. The SOFIE ice detection threshold corresponds to $M_{ice} \approx 0.06$ ng m^{-3} (depending slightly on AR). SOFIE indicates ice mass densities at Z_{max} ranging from 0.1 to 80 ng m^{-3}, with a mean value of 14.5 ng m^{-3} for the season (Fig 14a and Table 5). SOFIE is compared to the histogram of M_{ice} from ALOMAR lidar measurements (69°N) at Z_{max} during 2007, which indicates 2.8 to 245.5 ng m^{-3} with an average of 47.4 ng m^{-3}. PMC ice mass densities taken at Z_{max} in CARMA profiles according to Rapp and Thomas (2006) vary from 1 to 286 ng m^{-3}, generally encompassing the SOFIE results. Lidar results reported by von Cossart et al. (1999) indicate M_{ice} from 36 to 102 ng m^{-3}, and PMC measurements from the Halogen Occultation Experiment (HALOE) during 1992-2005 (e.g., Hervig et al., 2003) indicate M_{ice} from 24 to 200 ng m^{-3}. SOFIE indicates generally lower M_{ice} than the independent measurements in Fig. 14b. The relatively low mass densities from SOFIE are consistent with, but not wholly explained by, greater sensitivity of the SOFIE band 9 measurements compared to previous observations. The HALOE PMC detection threshold was $\beta(3.40) > 2\times10^{-6}$ km^{-1}, which corresponds to $M_{ice} > 13$ ng m^{-3}, or roughly a factor 200 times above the SOFIE PMC detection threshold. Thus, lower SOFIE mass densities compared to previous observations are at least partially explained by SOFIE observing more tenuous clouds. Nevertheless, enhanced sensitivity cannot entirely explain the differences because the SOFIE record does not contain $M_{ice} > 80$ ng m^{-3}, as indicated by the other observations. Remaining differences could be explained by averaging over the relatively large SOFIE FOV. As demonstrated in Fig. 12, vertical smoothing can reduce the peak extinction by up to 30%. It is also possible that the PMCs are not homogeneous over the 290 km horizontal SOFIE FOV dimension. For example, if identical PMC elements occupied only 50% of the SOFIE FOV, then the retrieved extinction would be underestimated by 50% because the path length calculations assume spherical homogeneity. Accounting for SOFIE measurement geometry generally explains the lack of higher mass densities in the SOFIE record. For example, if SOFIE mass densities are corrected assuming 30% reduction due to vertical FOV smoothing (e.g. Fig. 12) and 50% ice coverage within the LOS, the mean value of 14.9 ng m^{-3} becomes ~42 ng m^{-3}, consistent with the 2007 lidar observations. The effects of cloud inhomogeneity will be addressed in future studies using coincident hi-resolution PMC images from CIPS.

Particle axial ratios were determined using measurements of $\beta(3.064)/\beta(3.186)$ as described above. SOFIE indicates oblate spheroid axial ratios at Z_{max} predominately from about 1.5 to 3 with a mean value for all observations of 2.2 ± 0.5 (Fig. 14c and Table 5). The counterpart solutions for prolate spheroids (not shown) indicate *AR* from roughly 0.7 to 0.3. SOFIE is compared to a histogram of axial ratios determined from multi-color lidar measurements over ALOMAR In 2007 (Fig. 14c) (Baumgarten et al., 2008). The histogram of 2007 lidar results is similar to SOFIE, indicating *AR* predominately from about 1.2 to 3.5 and an average value of 2.1 ± 0.8. The main difference between SOFIE and the 2007 lidar results is that the lidar indicates more instances of $AR < 1.5$ and $AR > 3$ than SOFIE. This difference could be related to measurement/inversion errors, or differences in the clouds observed. The axial ratio of 2.5 reported by Baumgarten et al. (2002) based on lidar depolarization measurements is also shown in Fig. 14c. The 2007 SOFIE and lidar results are generally consistent with Eremenko et al. (2005) who indicate *AR* of about 2, but rarely approach the value of 5 reported by Rapp et al. (2007).

Effective radii were derived using measurements of $\beta(3.064)/\beta(1.037)$ with equation 4. These calculations assumed $AR = 2$, which induces negligible errors. SOFIE PMC effective radii at Z_{max} vary from about 5 to 80 nm and the mean value for all observations is 35.9 nm (Fig. 14b and Table 5). SOFIE results in Fig. 14b are compared to a histogram of effective radii at Z_{max} from the 2007 ALOMAR lidar measurements. Effective radii from the 2007 ALOMAR lidar results are in excellent agreement with SOFIE, indicating r_e from 14 to 80 nm with an average value of 37.9 nm. The primary difference between the 2007 SOFIE and lidar results is that

SOFIE indicates r_e < 15 nm while the lidar does not. Also shown in Fig 14b are the range of r_e reported from lidar measurements by von Cossart et al. (1999, Table 2 therein), satellite measurements (von Savigny et al., 2005; Rusch et al., 2007) and CARMA model calculations (Table 1 in Rapp and Thomas, 2006). These independent observations generally indicate r_e from about 25 to 80 nm, but not the smaller particles indicated by both SOFIE and the ALOMAR lidar in 2007. These differences could be due to seasonal variations in ice properties, and may also be related to greater sensitivity of SOFIE and the lidar, assuming that more tenuous clouds are characterized by smaller particles. SOFIE r_e estimates are not impacted by the effects of cloud inhomogeneity and/or FOV smoothing because these geometric errors are identical in each SOFIE bandpass.

It is important to note that particle size is only determined when $\beta(1.037)$ is above the noise, which corresponds to 48% of the observations with Z_{max} > 79 km. This occurs because 1.037 μm extinction is 50 to 20000 times lower than at 3.064 μm (see Fig. 8a), and ice is often identified in the IR measurements when no signal appears at 1.037 μm. This limitation also exists when determining size distributions in the absence of band 2. The measured $\beta(3.064)$ versus $\beta(3.064)/\beta(1.037)$ at Z_{max} is shown in Fig. 15, where a probability distribution of $\beta(3.064)$ is overlain. These results indicate that $\beta(1.037)$ (and therefore r_e) measurements are obtained predominately when $\beta(3.064) > \sim 10^{-5}$ km^{-1}. While the largest extinctions generally correspond to lower $\beta(3.064)/\beta(1.037)$ (and thus larger r_e), the data do not suggest a strict relationship. For example, $\beta(3.064)/\beta(1.037)$ varies by over two orders of magnitude (r_e from roughly 10 to 60 nm) for $\beta(3.064) = 5\times10^{-5}$ km^{-1}. Although SOFIE can rarely determine particle size for the most tenuous clouds, size is characterized over the dominant range of measurements.

Gaussian PMC size distribution parameters (N, r_m, and Δr) retrieved from SOFIE measurements at Z_{max} are summarized in Fig. 16 and Table 5. SOFIE results are compared to Gaussian size distributions retrieved at Z_{max} using ALOMAR RMR lidar observations during 2007. SOFIE concentrations range from 3 to 5342 cm^{-3} with an average of 394 cm^{-3} and a median value of 165 cm^{-3}. The lidar concentration range from 2 to 2668 cm^{-3} with an average of 228 cm^{-3} and a median value of 104 cm^{-3}. The generally lower concentrations from the lidar are accompanied by larger r_m, compared to SOFIE. The relationship between r_m and N for all SOFIE measurements at Z_{max} indicate that larger particles generally exist at lower concentrations (Fig. 17). When examining only measurements within a narrow range of extinction, the relationship between r_m and N is even more distinct. Differences in the distributions of r_m and N from SOFIE and from the lidar are therefore consistent with the SOFIE record containing smaller r_m. Indeed, if $r_m < 20$ nm are excluded from the SOFIE record, the average N becomes 168 cm^{-3}, much closer to the lidar value of 228 cm^{-3}. Excluding $r_m < 20$ nm from the SOFIE record gives an average $r_m = 33$ nm, still smaller than the lidar result. This persistent difference is related to more instances of $r_m > \sim 50$ nm in the lidar record than for SOFIE. The large separation between average and median concentration, and large standard deviations in N, result from the broad range of values that are observed. The typical definition of mean and standard deviation based on the Gaussian distribution may therefore not be applicable to statistical analysis of N. For comparison in Table 5, the standard deviations in N assuming a Poisson distribution are also given, indicating much smaller values. Particle concentrations from lidar measurements (von Cossart et al., 1999) and CARMA (Rapp and Thomas, 2006) generally encompass the 2007 SOFIE and ALOMAR lidar values. SOFIE indicates median radii from 7 to 100 nm with a mean value of 29.1 nm. The 2007 lidar results indicate r_m from 18 to 94 nm with an average value of

40.4 nm (Fig. 15b). Smaller r_m indicated in the SOFIE record are consistent with increased sensitivity to smaller particles, compared to the lidar. SOFIE distribution widths range from 5 to 23 nm with an average of 11.8 nm, in good agreement with the lidar results which indicate Δr from 4 to 24 nm with an average of 12.1 nm. Values of Δr from the modeling study of and Rapp and Thomas (2006) generally overlap the SOFIE and lidar results, but suggest larger values and lack Δr < 9 nm. While the theoretical uncertainties in SOFIE size distribution retrievals are increased in the absence of the band 2 UV measurements, the results presented here suggest that the SOFIE results are of sufficient quality for use in scientific studies.

7. Summary

This work establishes a basis for interpreting SOFIE observations and offers an initial assessment of SOFIE results from the northern summer of 2007. An analysis of the available ice refractive indices yields a reasonable approach to using these data, however, the need for new measurements covering UV – IR wavelengths at PMC temperatures is apparent. PMCs are readily identified in SOFIE observations using spectral information, and SOFIE indicates mesospheric ice existing as a continuous layer from 81.9 to 87.6 km on average. This result is consistent with model prediction, but previous observations indicate narrower ice layers due to lower sensitivity. Methods were presented for determining PMC ice mass density, particle shape, effective radius, and size distribution using SOFIE measurements. Analysis of SOFIE observations at the extinction peak during 2007 were presented and compared to previous and concurrent results. SOFIE indicates axial ratios of 1.5 to 3.0, consistent with concurrent lidar results but not with Rapp et al. (2007) who indicate AR = 5. SOFIE PMC mass densities are lower than previous observations, and this difference is consistent with greater sensitivity of the SOFIE instrument compared to previous instruments, but is also due to averaging by the relatively large SOFIE sample volume. SOFIE indicates effective radii that generally consistent with concurrent ALOMAR lidar measurements, although SOFIE indicates a class of effective radii from 5 to 15 nm that is not observed by the lidar. Gaussian size distributions were found to be generally consistent with concurrent lidar measurements from ALOMAR. Continued analyses of SOFIE PMC measurements from the northern summer of 2007 is offered by Hervig et al. (2008, this issue).

Acknowledgements. The AIM mission is supported by NASA's Small Explorer's Office. Thanks to the Space Dynamics Laboratory professionals, particularly Chad Fish, for years of diligent and careful effort in the design, construction, and testing the SOFIE instrument. Thanks to Chris Englert, Gary Thomas, Dave Rusch, and the rest of the AIM science team for collaboration and insight.

References

Alpers, M., M. Gerding, J. Höffner, and U. von Zahn, NLC particle properties from a five color lidar observation at 54°N, *J. Geophys. Res., 105,* 12,235-12,240, 2000.

Baumgarten, G., K. H. Fricke, and G. von Cossart, Investigation of the shape of noctilucent cloud particles by polarization lidar technique, *Geophys. Res. Lett.*, *29*(13), 1630, doi:10.1029/2001GL013877, 2002.

Baumgarten, G., G. von Cossart, and J. Fiedler, The size of noctilucent cloud particles above ALOMAR (69N,16E): Optical modeling and method description, Adv. Space Res., Volume 40, Issue 6, p. 772-784, doi:10.1016/j.asr.2007.01.018, 2007.

Baumgarten, G., J. Fiedler, F.-J. Lübken, and G. von Cossart, Interannual variations of particle properties and water content of noctilucent clouds, *J. Geophys. Res., in press,* 2008.

Baumgarten, G., and J. Fiedler, Vertical structure of particle properties and water content in noctilucent clouds, *Geophys. Res. Letters, in review,* 2008.

Bertie, J. E., H. J. Labbe, and E. Whalley, Absorptivity of ice I in the Range 4000-30 cm^{-1}, *J. Chem. Phys*., *50*, 4501-4520, 1969.

Clapp, M. L., R. E. Miller, and D. R. Worsnop, Frequency-dependent optical constants of water ice obtained directly from aerosol extinction spectra, *J. Phys. Chem., 99*, 6317, 1995.

Gordley, L.L., M.E. Hervig, J.M. Russell III, C. Fish, G.J. Paxton, J.C. Burton, and M.J. McHugh, Sounding the upper mesosphere using broadband solar occultation: the SOFIE experiment, *Proc. SPIE Vol. 6297,* 62970G, 2006.

Gordley, L.L., M. Hervig, C. Fish, et al., The Solar Occultation For Ice Experiment, *J. Atmos. and Solar-Terrestrial Phys.*, in review, 2007.

Gosse, S., D. Labrie, and P. Chylek, Refractive index of ice in the 1.4-7.8-mm spectral range, *Applied optics*, *34*, 6582-6586, 1995.

Hervig, M. E., R. E. Thompson, M. McHugh, L. L. Gordley, J. M. Russell III, and M. E. Summers, First confirmation that water ice is the primary component of polar mesospheric clouds, *Geophys. Res. Letters, 28*, 971-974, 2001.

Hervig, M., M. McHugh, and M. Summers, Water vapor enhancement in the polar summer mesosphere and its relationship to polar mesospheric clouds, *Geophys. Res. Letters*, *30(20)*, 2041, doi:10.1029/2003GL018089, 2003.

Hervig, M.E., L.L. Gordley, M. Stevens, J.M. Russell, and S. Bailey, SOFIE PMC measurements during the northern summer of 2007, *J. Atmos. Solar-Terr. Phys.*, in review, 2008.

Lübken, F.-J., Thermal structure of the Arctic summer mesosphere, *J. Geophys. Res.*, *104* (D8), 9135, 1999.

Mishchenko, M. I., and L. D. Travis (1998), Capabilities and limitations of a current FORTRAN implementation of the T-matrix method for randomly oriented, rotationally symmetric scatterers, J. Quant. Spectrosc. Radiat. Transfer, 60, 309 – 324.

Petrenko, and Whitworth, Physics of Ice, *Oxford Univ. Press*, New York, 1999.

Pruppacher, H. R. and J. D. Klett, Microphysics of Clouds and Precipitation, D. Reidel, Norwell, Mass., 1980.

Rajaram B., D.L. Glandorf, D.B. Curtis, M.A. Tolbert, O.B. Toon, N. Ockman, Temperature-dependent optical constants of water ice in the near infrared: new results and critical review of the available measurements, *Applied Optics*, *40*, 4449-4462, 2001.

Rapp, M. and F.-J. Lübken, Polar mesosphere summer echoes (PMSE): review of observations and current understanding, *Atmos. Chem. Phys.*, 4, 2601–2633, SRef-ID: 1680-7324/acp/2004-4-2601, 2004.

Rapp, M., and G. E. Thomas, Modeling the microphysics of mesospheric ice particles: Assessment of current capabilities and basic sensitivities, *J. Atmos. and Solar-Terrestrial Phys.*, doi:10.1016/j.jastp.2005.10.015, 2006.

Rapp, M., G. E. Thomas, and G. Baumgarten, Spectral properties of mesospheric ice clouds: Evidence for nonspherical particles, *J. Geophys. Res.*, *112*, D03211, doi:10.1029/2006JD007322, 2007.

Rusch, D. W., G. E. Thomas, and E. J. Jensen, Particle size distributions in polar mesospheric clouds derived from solar mesosphere explorer measurements, *J. Geophys. Res., 96,* 12,933-12,939, 1991.

Rusch, D.W., S.M. Bailey, G.E. Thomas, and A.W. Merkel, Seasonal-latitudinal Variations of PMC Particle Size from SME Measurements for the Northern 1983 Season and SNOE

Measurements for the Northern 2000 and Southern 2000/2001 Seasons, *J. Geophys. Res., in press, 2007.*

Russell, J. M. III, S. M. Bailey, M. Horányi, L. L. Gordley, D. W. Rusch, M. E. Hervig, G. E. Thomas, C. E. Randall, W. E. McClintock, D. E. Siskind, M. H. Stevens, M. E. Summers, M. J. Taylor, C. R. Englert, P. J. Espy, and A. W. Merkel, Aeronomy of Ice in the Mesosphere (AIM): A satellite mission to study polar mesospheric clouds, *IEEE Transactions on Aerospace and Electronic Systems, in review*, 2008.

Siskind, D. E., M. H. Stevens, and C. R. Englert, A model study of global variability in mesospheric cloudiness, *J. Atmos. and Solar-Terrestrial Phys.*, doi:10.1016/jastp.2004.11.007, 2005.

Toon O. B., M. A. Tolbert, B. G. Koehler, A. M. Middlebrook, and J. Jordan, Infrared optical constants of H_2O ice, amorphous nitric acid solutions, and nitric acid hydrates, *J. Geophys. Res.*, *99*, 25,631-25,645, 1994.

von Cossart, G., J. Fiedler, and U. von Zahn, Size distributions of NLC particles as determined from 3-color observations of NLC by ground-based lidar, *Geophys. Res. Lett., 26,* 1513-1516, 1999.

von Savigny, C., S. V. Petelina, B. Karlsson, E. J. Llewellyn, D. A. Degenstein, N. D. Lloyd, and J. P. Burrows (2005), Vertical variation of NLC particle sizes retrieved from Odin/OSIRIS limb scattering observations, *Geophys. Res. Lett.*, *32*, L07806, doi:10.1029/2004GL021982.

Warren, S. G., Optical constants of ice from the ultraviolet to the microwave, *Appl. Optics*, *23*, 11.906-11.926, 1984.

Table 1.
Ice refractive index data considered in this work.

Reference	Wavelengths (μm)	Temperature (K)	Comment
Bertie et al. (1969)	1.2 - 333	100	
Clapp et al. (1995)	2.5 – 12.5	130 - 210	10 K interval
Toon et al. (1994)	1.4 - 20	163	
Rajaram et al. (2001)	1.4 – 2.7	166 - 196	10 K interval
Gosse et al. (1995)	1.4 – 7.8	251	Imaginary index only
Warren (1984)	0.05 - 2000	266	Based on many data sets

Table 2.
Ice refractive index for each SOFIE wavelength. Values for bands 5-16 were taken at 145 K from polynomial fits to the available indices versus temperature, and the listed uncertainties are from the standard error in the regression. The values for bands 1-4 are from Warren (1984).

Band	Wavelength (μm)	Real Index	Imaginary Index
1	0.292	1.354	8.433×10^{-9}
2_p	0.330	1.335	5.375×10^{-9}
3_p	0.867	1.304	2.500×10^{-7}
4_p	1.037	1.301	2.330×10^{-6}
5_p	2.462	$1.237 \pm 2.51\times10^{-3}$	$5.611 \times 10^{-4} \pm 8.67\times10^{-5}$
6	2.618	$1.202 \pm 4.41\times10^{-3}$	$5.041 \times 10^{-3} \pm 1.72\times10^{-4}$
7	2.785	$1.111 \pm 6.99\times10^{-3}$	$1.066 \times 10^{-2} \pm 4.04\times10^{-3}$
8_p	2.939	$0.910 \pm 3.23\times10^{-2}$	$2.600 \times 10^{-1} \pm 1.75\times10^{-2}$
9_p	3.064	$1.022 \pm 3.98\times10^{-2}$	$7.007 \times 10^{-1} \pm 3.84\times10^{-2}$
10_p	3.186	$1.759 \pm 3.07\times10^{-2}$	$5.372 \times 10^{-1} \pm 4.22\times10^{-2}$
11_p	3.384	$1.566 \pm 2.47\times10^{-2}$	$3.427 \times 10^{-2} \pm 2.94\times10^{-3}$
12_p	3.479	$1.500 \pm 2.17\times10^{-2}$	$1.286 \times 10^{-2} \pm 1.19\times10^{-3}$
13	4.324	$1.370 \pm 7.83\times10^{-3}$	$2.749 \times 10^{-2} \pm 1.67\times10^{-3}$
14_p	4.646	$1.379 \pm 9.01\times10^{-3}$	$2.468 \times 10^{-2} \pm 1.24\times10^{-3}$
15_p	5.006	$1.360 \pm 8.15\times10^{-3}$	$1.193 \times 10^{-2} \pm 1.14\times10^{-3}$
16	5.316	$1.340 \pm 7.68\times10^{-3}$	$1.695 \times 10^{-2} \pm 1.25\times10^{-3}$

[1]subscript p indicates bands intended for PMC retrievals.

Table 3.
The constants $A_0(\lambda)$ and $B(\lambda)$ for Equation 2 and uncertainty in $A(\lambda)$ for infrared SOFIE wavelengths. Results are based on the ice indices in Table 2.

Band[1]	λ (μm)	$A_0(\lambda)$ (μm^3 cm^{-3} km)	$B(\lambda)$ (μm^3 cm^{-3})	**Uncertainty in** $A(\lambda)$ **(%)**
5_p	2.462	2.735×10^5	-2045.1	28.9
6	2.616	3.462×10^5	-1880.7	23.9
7	2.785	2.155×10^4	-44.9	10.2
8_p	2.939	8.645×10^2	3.0	2.0
9_p	3.064	3.228×10^2	10.4	1.9
10_p	3.186	7.744×10^2	-59.3	2.6
11_p	3.384	1.068×10^4	-480.9	3.8
12_p	3.479	2.743×10^4	-1008.1	5.1
13	4.324	1.509×10^4	-332.9	2.0
14_p	4.646	1.819×10^4	-419.4	1.7
15_p	5.006	3.995×10^4	-840.4	3.0
16	5.316	2.960×10^4	-565.4	2.2

[1]subscript p indicates bands intended for PMC retrievals.

Table 4.
Constants for equation 4 for various axial ratios and two extinction ratios.

AR	a_1	a_2	a_3	a_4	a_5
			β(3.06)/β(1.04)		
1	2.15982	0.394180	-0.498117	0.129728	-0.0116792
2	2.17598	0.373915	-0.493485	0.129914	-0.0117900
3	2.20024	0.344996	-0.486569	0.130015	-0.0119260
			β(3.06)/β(0.867)		
1	2.36665	-0.142000	-0.195199	0.0579987	-0.00546634
2	2.38181	-0.164386	-0.187591	0.0571021	-0.00545287
3	2.40662	-0.198723	-0.175434	0.0554889	-0.00540229

Table 5.
Summary of 2007 Northern Summer PMC Observations from SOFIE and from the ALOMAR lidar. SOFIE results considered only PMCs with Z_{max} > 79 km. Microphysical cloud properties are for Z_{max}.

	SOFIE			ALOMAR lidar		
Parameter	Mean	Median	Standard deviation	Mean	Median	Standard Deviation
Z_{top} (km)	87.6	87.8	1.7	84.4	84.4	1.4
Z_{max} (km)	83.8	83.8	1.8	83.3	83.3	1.3
Z_{bot} (km)	81.9	81.6	1.6	82.2	82.2	1.4
$Z_{top} - Z_{bot}$ (km)	5.7	5.6	2.0	2.2	2.2	1.4
AR_O	2.3	2.2	0.6	2.1	2.1	0.8
M_{ice} (ng m^{-3})	14.5	10.1	14.3	47.4	40.9	27.9
r_e (nm)	35.9	34.7	14.9	37.9	35.0	14.5
N (cm^{-3})	373.7	164.5	660.7 (19.8*)	227.5	104.3	213.5 (15.1*)
r_m (nm)	29.0	28.4	11.3	40.4	35.7	15.6
Δr (nm)	11.8	11.5	3.4	12.1	11.6	3.3

*The standard deviation of a Poisson distribution.

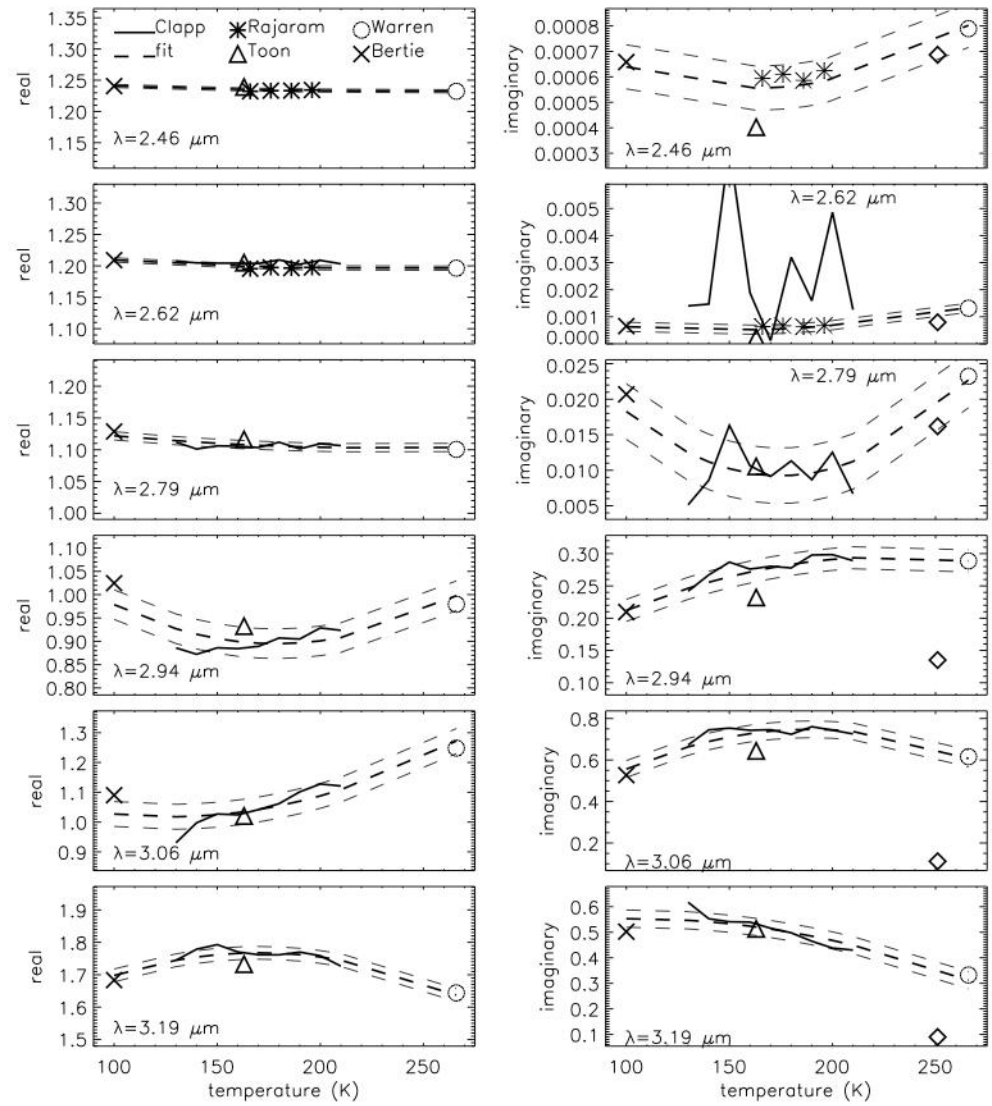

Fig. 1. The real and imaginary ice refractive index versus temperature for SOFIE wavelengths greater than 2.4 μm, from the references in Table 1. Data from Rajaram et al. (2001) (*) were only available for bands 5 and 6 (2.46 and 2.62 μm), and data from all references were available only at 2.62 μm. Gosse et al. (1995) (251 K) did not report the real index. Second order polynomial fits to the data are shown. Note that the Gosse et al. indices were not included in the polynomial fits, and that the Clapp et al. (1995) imaginary indices were not used at 2.62 μm.

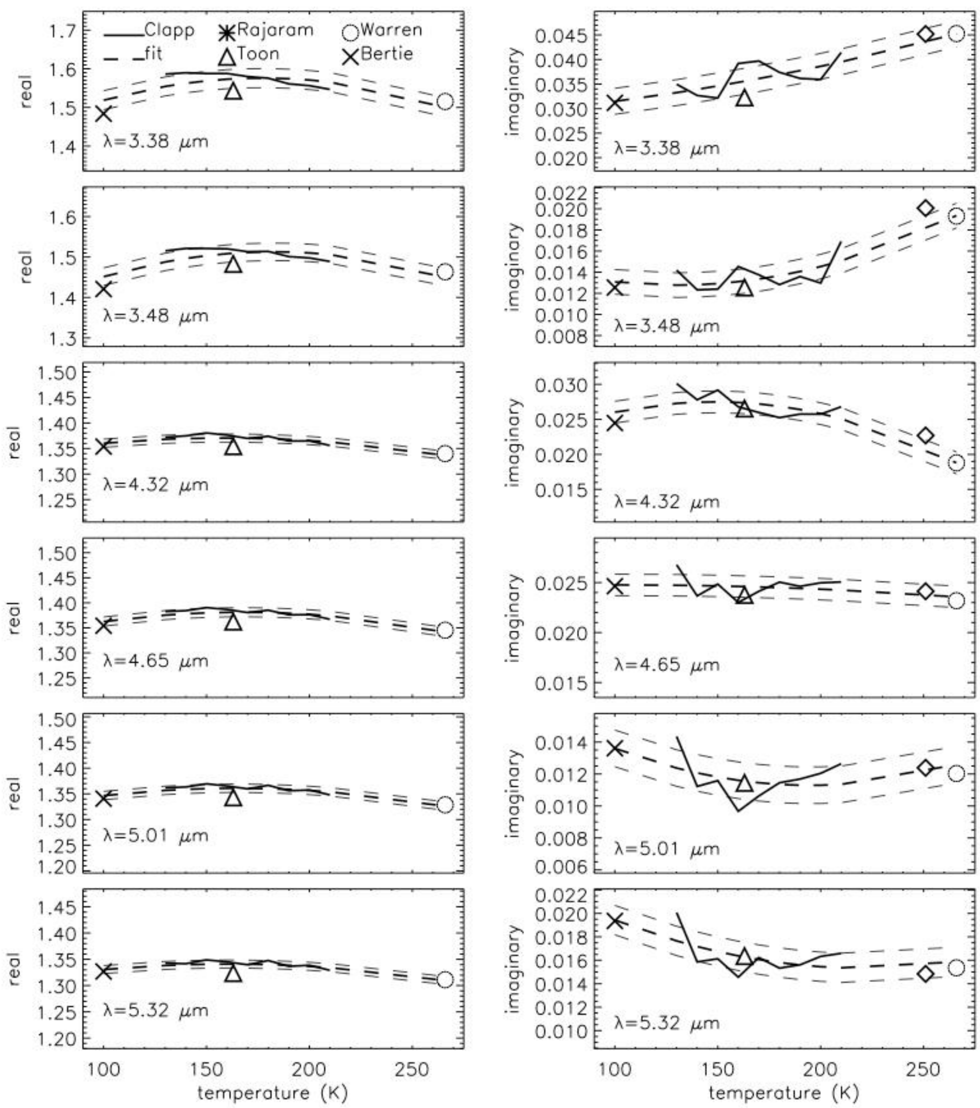

Fig. 1. Continued.

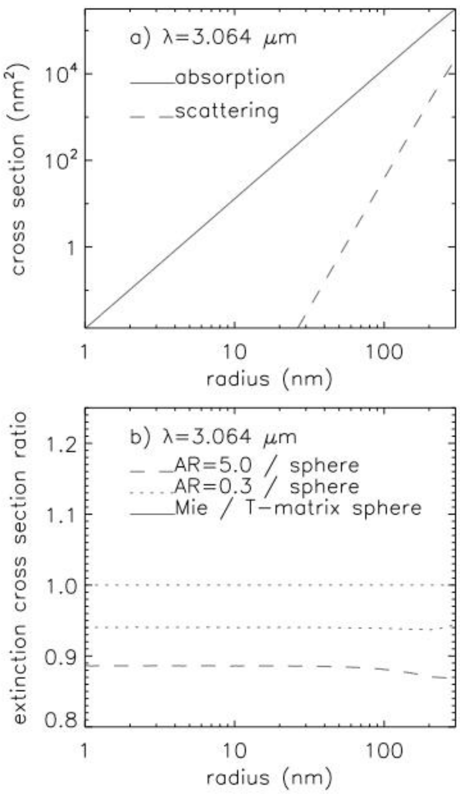

Fig. 2. a) Modeled particle scattering and absorption cross section at 3.064 μm wavelength versus particle radius for spheres using the ice refractive index in Table 2. b) The ratio of extinction cross sections at 3.064 μm wavelength for oblate and prolate spheroids compared to results for spheres. Mie cross sections are compared to T-matrix results for a spherical particle (*AR*=1).

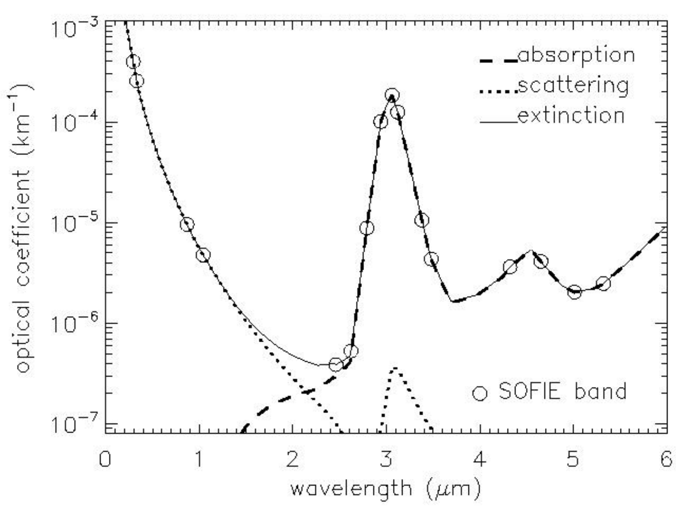

Fig. 3. PMC absorption, scattering, and extinction, calculated using Mie theory with ice refractive indices as in Table 2 and the average PMC size distribution from von Cossart et al. (1999). SOFIE band locations are indicated.

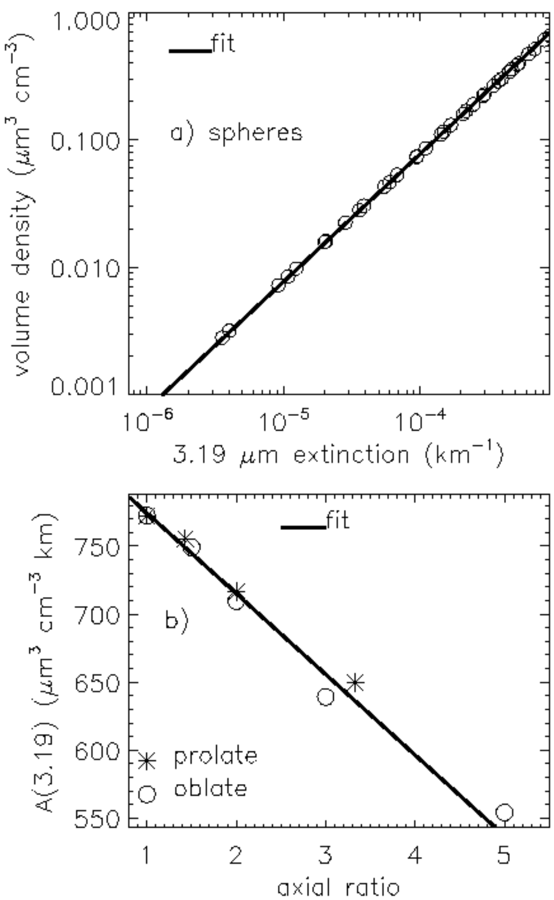

Fig. 4. a) Calculated PMC extinction versus volume density for SOFIE band 10. The calculations are for spheres (*AR*=1), ice refractive indices as in Table 2, and Gaussian size distributions with N = 80 cm^{-3}, median radii from 10 to 100 nm, and distribution widths from 5 to 25 nm. A fit to the data is shown. b) The constant, $A(\lambda)$ from equation 1 as a function of axial ratio. Values for prolate spheroids are located at $1/AR_P$ on the ordinate. A fit to $A(\lambda)$ versus *AR* is shown.

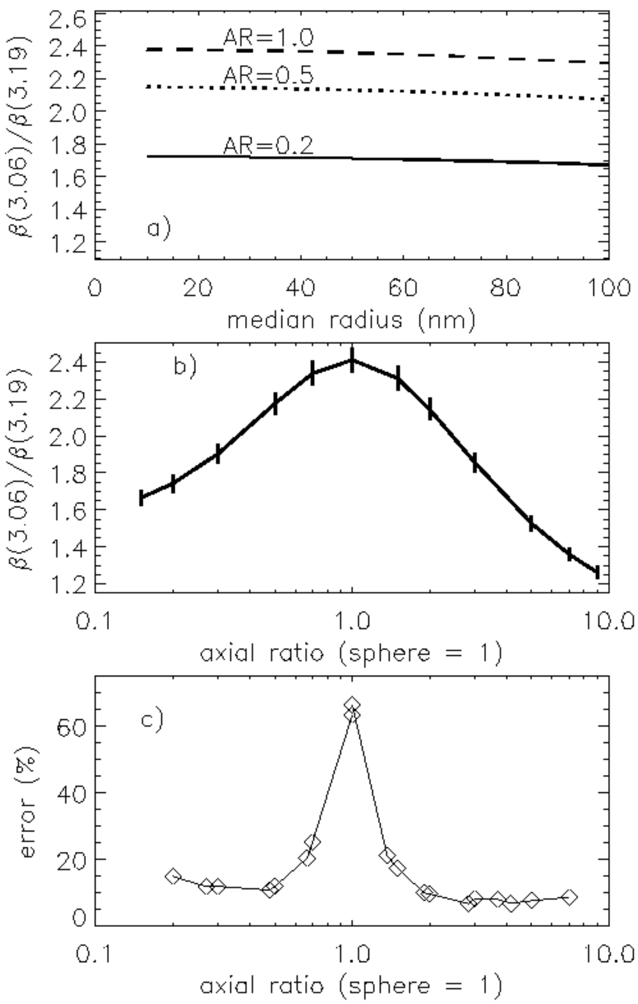

Fig. 5. a) Calculated extinction ratio, $\beta(3.064)/\beta(3.186)$, versus the median radius of a Gaussian distribution with Δr = 15 nm. The calculations used the ice refractive indices in Table 2 and various particle axial ratios as indicated. b) Extinction ratio versus axial ratio. Vertical bars indicate uncertainty due to unknown particle size and uncertainty in the ice refractive indices. c) The uncertainty in inferred axial ratio due to uncertainties in the modeled relationship between AR and $\beta(3.064)/\beta(3.186)$.

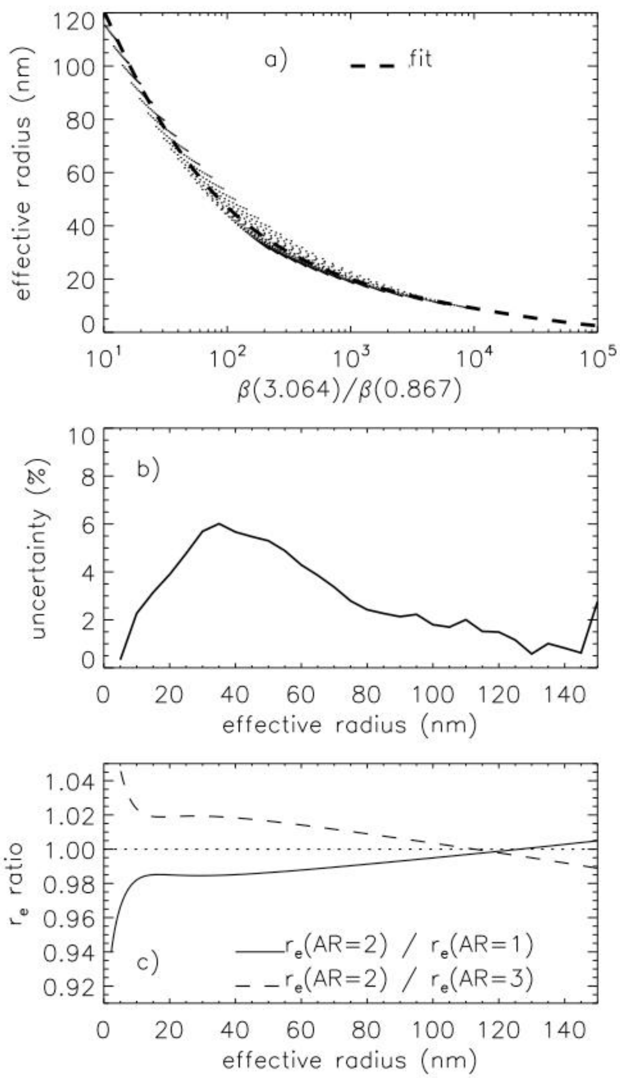

Fig. 6. a) The relationship between effective radius and the extinction ratio, R_{94} = $\beta(3.064)/\beta(0.867)$, from model calculations considering AR = 2 and Gaussian size distributions with $2 < r_m < 150$ nm and $5 < \Delta r < 20$ nm. A fit to the model results is shown. b) Uncertainty in the fit to r_e versus R_{93} in Fig. 6a. c) The ratio of R_e determined for AR = 2, $r_e(AR=2)$, to that determined for AR = 1 or 3, as a function of $r_e(AR=2)$.

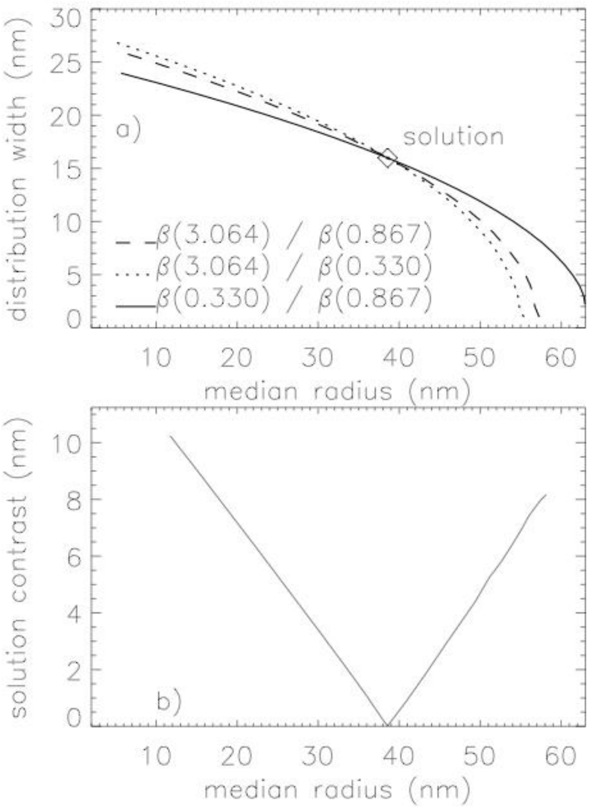

Fig. 7. a) The curves represent all pairs of r_m and Δr that can explain an extinction ratio calculated for r_m =38.5 nm and Δr = 16 nm. Results are for combinations using bands 2, 3, and 9. The solution is identified at the intersection of the three curves (diamond). b) Contrast among the solution curves in Fig. 7a as the spread in possible values of r_m versus the average r_m at a given Δr.

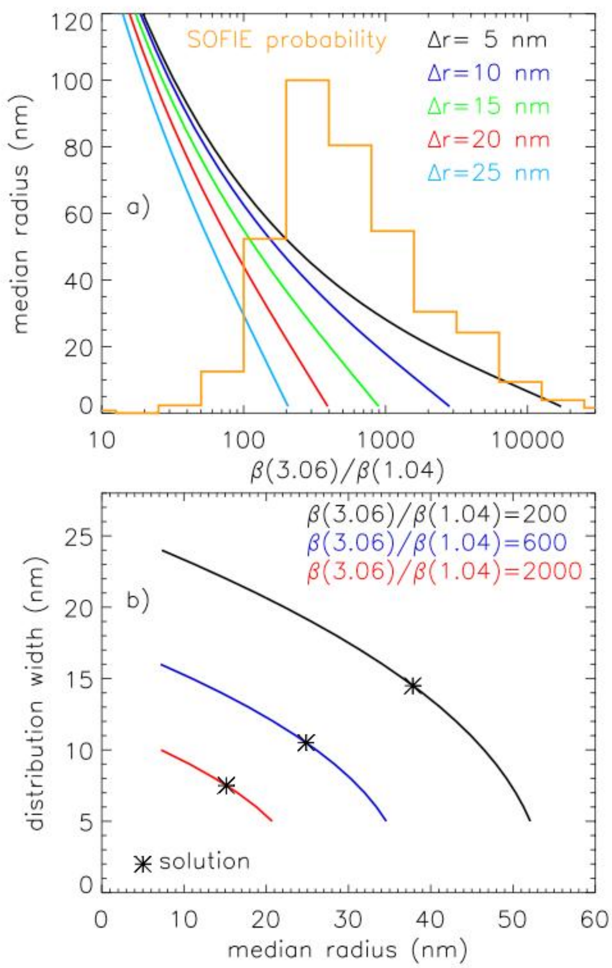

Fig. 8. Model calculations considering Gaussian size distributions and refractive indices for 145 K showing a) extinction ratio $\beta(3.064)/\beta(1.037)$ versus median radius for distribution widths as labeled. The probability distribution for SOFIE extinction ratio measurements at Z_{max} in the northern hemisphere during 2007 are overlain (the probability magnitude is arbitrary). b) The range of solutions (r_m versus Δr) corresponding to extinction ratios of 200, 600, and 2000. The solution taken at the mid-point of the possible widths is indicated.

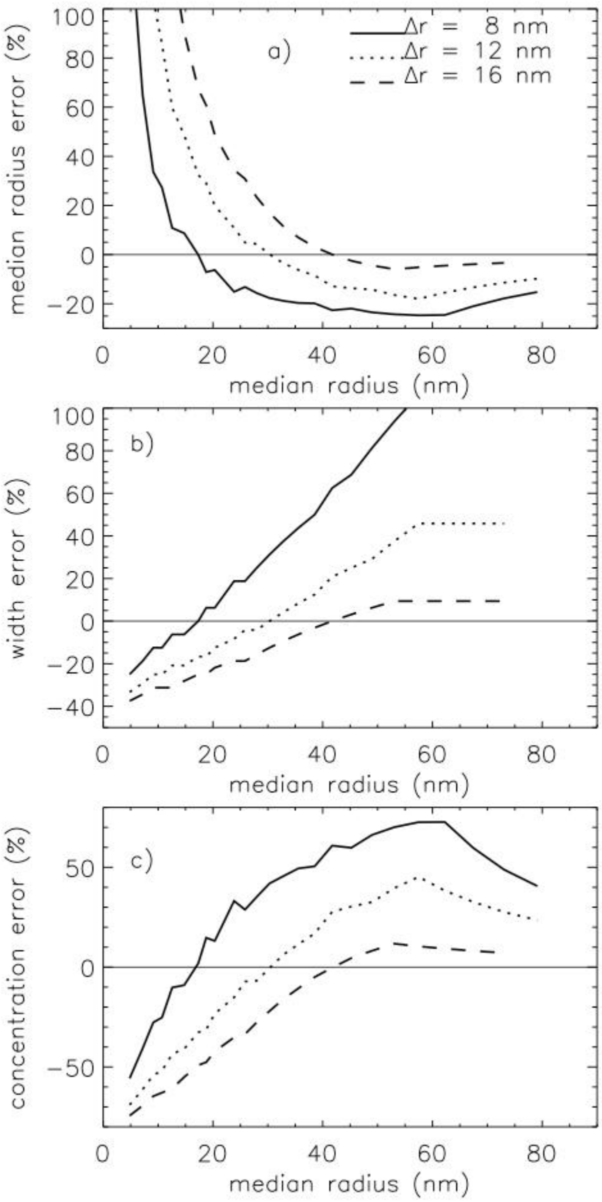

Fig. 9. Errors in the retrieved Gaussian size distribution median radius (a), width (b), and concentration (c), when the solution is taken as the midpoint of all possible solutions defined by $\beta(3.064)/\beta(1.037)$. The results used values of $\beta(3.064)/\beta(1.037)$ from 50 to 20000, and are shown versus median radius for three different widths as labeled.

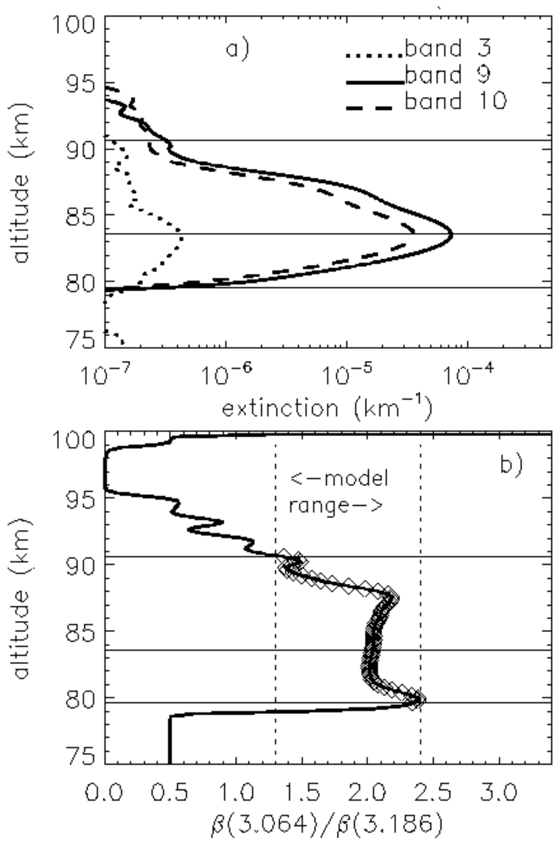

Fig. 10. SOFIE measurements on 9 July 2007, 21:39 UT, at 66.8°N, 20.0°E. Altitude of the ice layer top, peak, and base are indicated by thin horizontal lines. a) Extinction profiles from bands 3 (1.037 μm), 9 (3.064 μm) and 10 (3.186 μm). b) The ratio of $\beta(3.064)/\beta(1.037)$ with the predicted range that is consistent with PMC particles as indicated by vertical dotted lines. Measurements that are above twice the noise and consistent with predicted PMC extinction ratios are indicated by diamonds.

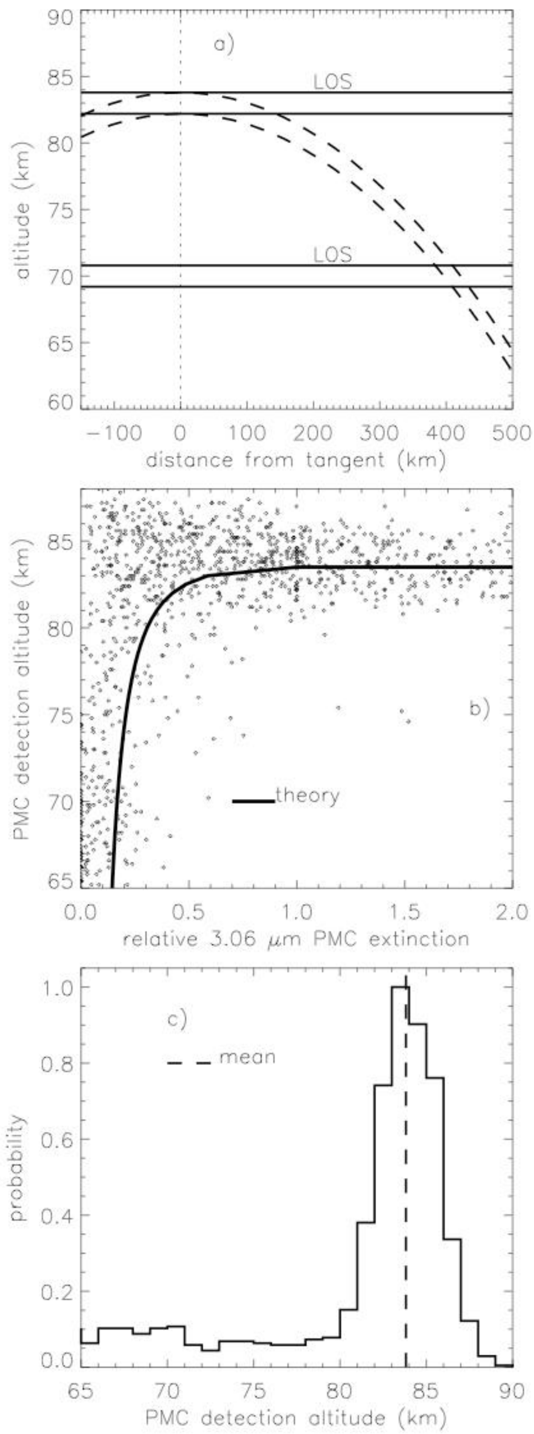

Fig. 11. a) The SOFIE line-of-sight (1.5 km thick) depicted at 83 and 70 km intercepting a 1.5 km thick cloud layer at 83 km altitude (dashed lines). The tangent point location is indicated (dotted line). The illustration is not true to scale. b) SOFIE PMC extinction at Z_{max} normalized to the median cloud extinction observed on the same day with Z_{max} between 80 and 85 km, shown as a function of Z_{max}. The results are for every PMC observed in the northern 2007 summer and are compared to a theoretical prediction considering cloud elements isolated where the line-of-sight intercepts the 83.5 km atmospheric shell. b) Probability distribution of Z_{max} for all northern 2007 SOFIE PMC observations.

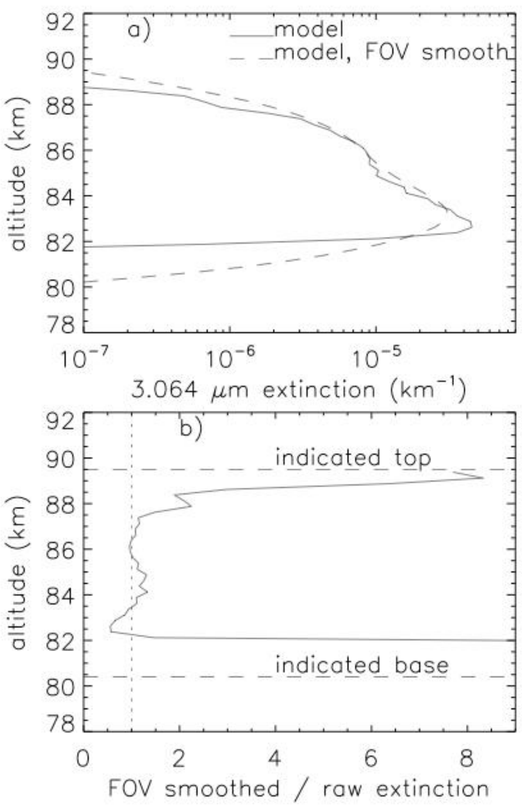

Fig. 12. a) 3.064 μm extinction computed from CARMA model PMC size distributions and the profile after smoothing over the SOFIE band 9 FOV. b) The ratio of smoothed to original extinction profiles. The altitude of cloud top and base that would be indicated by the smoothed profile are indicated.

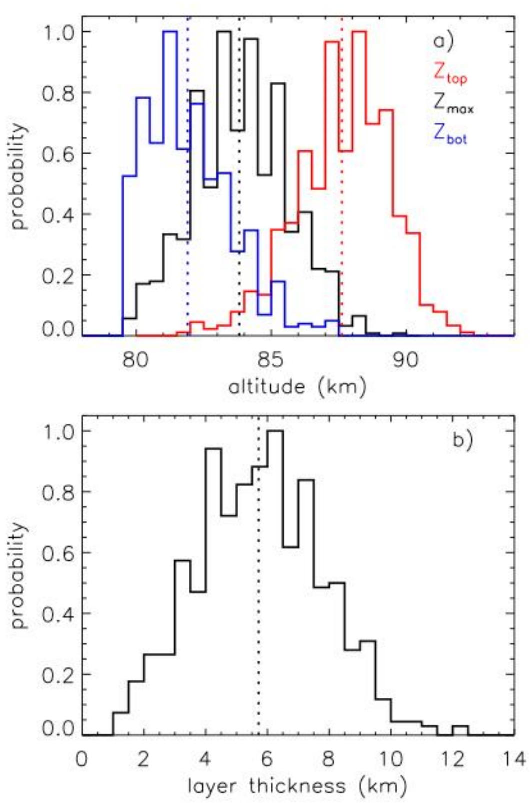

Fig. 13. a) probability distributions of PMC top, peak, and base altitude based on all cloud observations from the northern summer of 2007. Vertical dotted lines indicate the average SOFIE values. b) Probability distribution of the ice layer thickness (Z_{top} – Z_{bot}). In all cases ice observations with Z_{bot} or Z_{max} below 79 km were excluded.

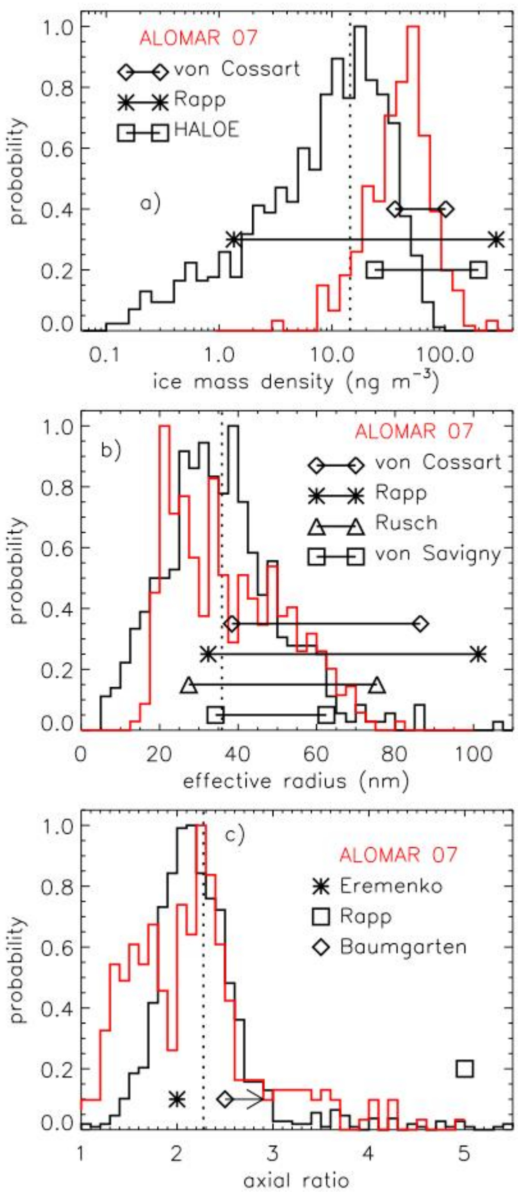

Fig. 14. Probability distributions of PMC properties determined from SOFIE observations at Z_{max} during the northern summer of 2007 (black lines). Average SOFIE values are indicated by vertical dotted lines. Probability distributions from ALOMAR lidar results at Z_{max} during 2007 are overlain in all cases The range of other independent results at Z_{max} are arbitrarily located on the ordinate. a) SOFIE mass density compared to the range of lidar results from von Cossart et al. (1999), model results from Rapp and Thomas (2006), and HALOE results during 1992-2005. b) SOFIE effective radius compared to the range of values from von Cossart et al. (1999), Rapp and Thomas (2006), Rusch et al. (2007), and von Savigny et al. (2005). c) The distribution of SOFIE axial ratios compared to axial ratios from Eremenko et al. (2005), Rapp et al. (2007), and Baumgarten et al., (2002).

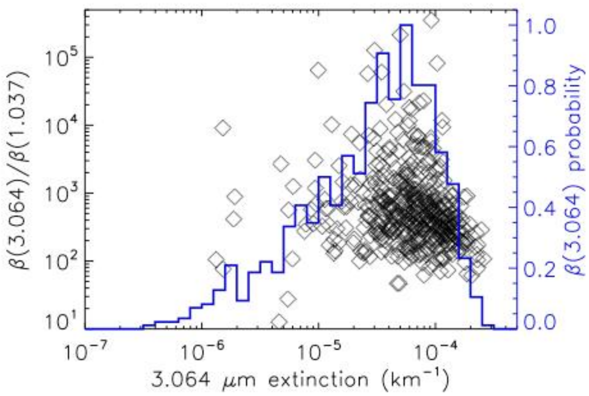

Fig. 15. β(3.064) versus β(3.064)/β(1.037) measured at Z_{max}. A probability distribution of β(3.064) measured at Z_{max} is overlain.

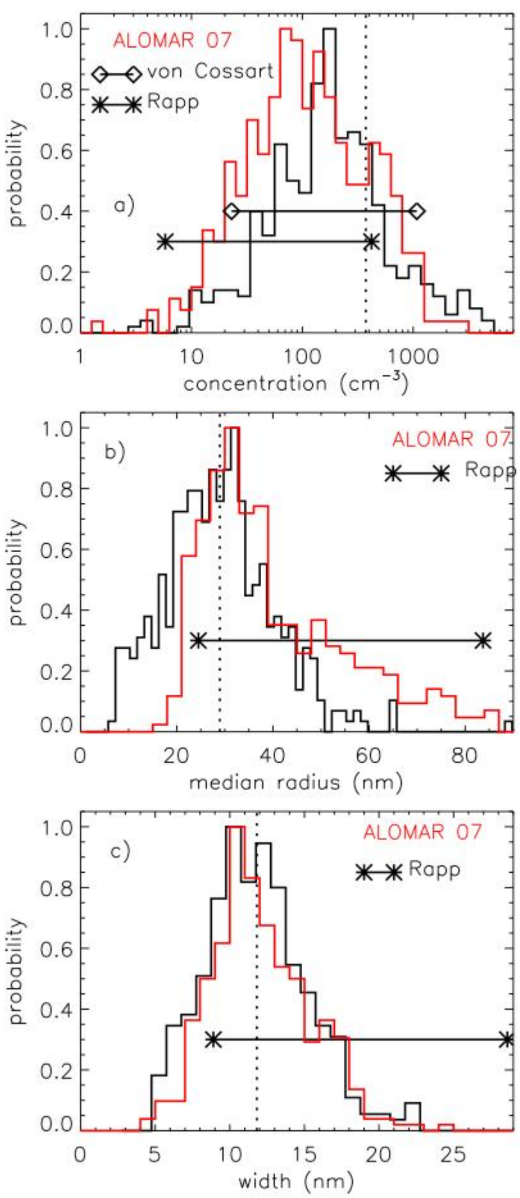

Fig. 16. Probability distributions of the Gaussian size distribution a) concentration, b) median radius, and c) width, retrieved from SOFIE measurements at Z_{max} in the northern hemisphere during 2007 (black lines). SOFIE results are compared to the distribution of results obtained at Z_{max} from lidar measurements over ALOMAR in 2007. Average SOFIE values are indicated by vertical dotted lines. The range of model size distribution parameters from Rapp et al. (2007), and concentration from lidar results reported by von Cossart et al. (1999) are indicated. These independent results are arbitrarily located on the ordinate.

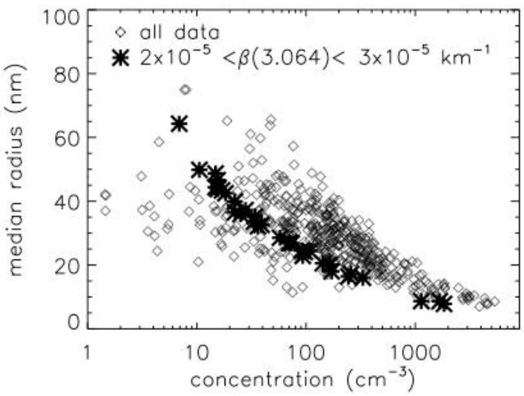

Fig. 17. Concentration versus median radius at Z_{max} for all 2007 SOFIE observations, and only those with 3.064 μm extinctions between 2×10^{-5} and 3×10^{-5} km^{-1}.